JASA ARTICLE

Soft elastomers: A playground for guided waves[a)]

Alexandre Delory,[1,b)] Fabrice Lemoult,[1,c)] Maxime Lanoy,[1,d)] Antonin Eddi,[2] and Claire Prada[1]

[1]*Institut Langevin, ESPCI Paris, Université PSL, CNRS, 75005 Paris, France*

[2]*Laboratoire Physique et Mécanique des Milieux Hétérogènes, CNRS, ESPCI Paris, Université PSL, Sorbonne Université, Université de Paris, 75005 Paris, France*

ABSTRACT:
Mechanical waves propagating in soft materials play an important role in physiology. They can be natural, such as the cochlear wave in the inner ear of mammalians, or controlled, such as in elastography in the context of medical imaging. In a recent study, Lanoy, Lemoult, Eddi, and Prada [Proc. Natl. Acad. Sci. U.S.A. **117**(48), 30186–30190 (2020)] implemented an experimental tabletop platform that allows direct observation of in-plane guided waves in a soft strip. Here, a detailed description of the setup and signal processing steps is presented as well as the theoretical framework supporting them. One motivation is to propose a tutorial experiment for visualizing the propagation of guided elastic waves. Last, the versatility of the experimental platform is exploited to illustrate experimentally original features of wave physics, such as backward modes, stationary modes, and Dirac cones.
 https://doi.org/10.1121/10.0011391

(Received 6 December 2021; revised 25 April 2022; accepted 25 April 2022; published online 20 May 2022)

[Editor: Preston Scot Wilson] Pages: 3343–3358

I. INTRODUCTION

The mechanical behavior of soft materials plays a crucial role in various physiological processes.[1] For example, the impact of the local stiffness of tissues during their development,[2] the stiffening of a tumor cell,[3] and the non-linear softening of arteries[4] are customary mechanisms still under investigation. Most biological tissues are *soft* and nearly *incompressible*. Mimicking them requires fulfillment of these two mechanical properties. In that regard, elastomers are interesting candidates. Indeed, they cover a wide range of mechanical properties, and they can be moulded into an infinite variety of shapes. In plastic surgery, silicone rubber has been adopted to reproduce the shapes and mechanical properties of breasts, lips, or noses. In the cinema industry, they have become a standard to form skin-masks. Nowadays, silicone elastomers seem to be promising materials to build artificial organs (such as vocal folds[5] or hearts[6]), soft robots,[7,8] or even baromorph materials.[9,10]

Due to their nearly incompressible nature, these soft materials present interesting dynamical properties involved in the propagation of elastic waves: the longitudinal waves are several orders of magnitude faster than their transverse counterpart ($V_L \gg V_T$). This specificity has enabled the development of transient elastography,[11] which is now clinically used for liver cirrhosis[12] or tumor detection.[13] However, elastography is not quantitative when it deals with narrow targets, such as artery walls,[14–16] the myocardium,[17,18] the Achilles' tendon,[19] or even biofilms.[20] In these geometries, the edges induce guiding phenomena, thus resulting in different apparent wave velocities. Guided elastic waves are also naturally involved in physiological processes. At the cellular scale, pressure pulses are observed in lipid monolayers,[21] and at the macroscopic scale, the vocal cords are the support of stationary waves.[22] Another compelling example is the sound transduction operated by the inner ear of mammalians: the *cochlear wave* is a guided mechanical wave that travels along the basilar membrane.[23,24]

Although guiding is a universal wave phenomenon, the case of elastic waves is particularly fascinating: up to three different polarizations can couple at each reflection,[25] and at least two distinct wave velocities are involved. Even in a geometry as simple as a plate, elastic guided waves present original properties. These waves have been extensively studied, especially for non-destructive testing applications.[26,27] Under certain conditions, they display unique features, such as negative phase velocities[28,29] or zero-group velocity (ZGV).[30–33]

This article presents a detailed experimental and theoretical framework for the investigation of the in-plane motion in soft waveguides. First, an experimental platform designed to track the in-plane displacement of a thin plate is proposed. The corresponding theoretical background (Rayleigh–Lamb equation) is exposed. Then an equivalence between Lamb modes and the in-plane motion of a thin strip is made. The strip configuration is investigated experimentally as well. Unique wave features, such as a backward mode, a ZGV point, and a Dirac cone in the $k \to 0$ limit, are

[a)]This paper is part of a special issue on Education in Acoustics.
[b)]Also at: PMMH, CNRS, ESPCI Paris, Université PSL, Sorbonne Université, Université de Paris, 75005 Paris, France.
[c)]Electronic mail: fabrice.lemoult@espci.psl.eu
[d)]Current address: Laboratoire d'Acoustique de l'Université du Mans (LAUM), UMR 6613, Institut d'Acoustique - Graduate School (IA-GS), CNRS, Le Mans Université, 72085 Le Mans, France.

https://doi.org/10.1121/10.0011391

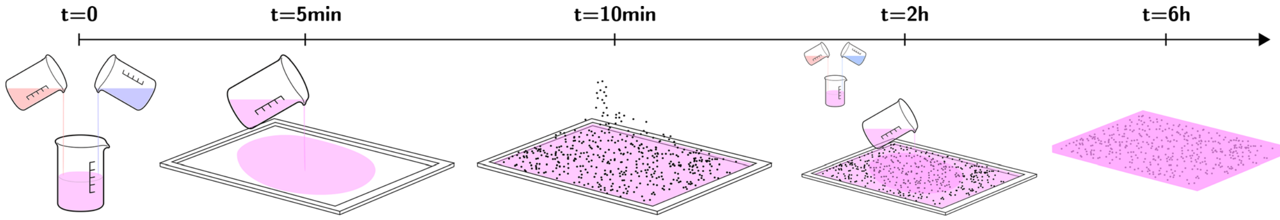

FIG. 1. (Color online) Ecoflex® sample preparation. At time $t=0$, the monomer and its cross-linking agent are mixed in equal proportions, and a first layer is poured in the sample mould. At $t=10$ min, the sample is sprinkled with black carbon grains dedicated to the displacement tracking. At $t=2$ h, a second layer is poured and cures for 6 h until complete cross-linking.

reported.[34] As such, the soft strip appears as an appropriate tutorial configuration to expose the richness of linear elastodynamics. Finally, it is demonstrated how the mode chirality can be exploited to perform selective excitation.

II. LOW FREQUENCY IN-PLANE GUIDED WAVES IN A SOFT PLATE

This section examines the vibration of a thin plate made of a nearly incompressible material. The experimental procedure is detailed, and the measured in-plane fields are presented. Then the theory supporting these measurements is provided, recalling how the reflections of bulk elastic waves at a free interface lead to the emergence of shear horizontal guided waves and Lamb waves.

A. Experiments

The soft plate preparation and the experimental platform are described. Then the stroboscopic image acquisition and post-processing operations are explained, and the resulting in-plane wave-fields are discussed.

1. Sample preparation

Throughout this article, the selected soft elastomer is the silicone rubber Smooth-On Ecoflex® 00-30, a material that has been widely used in academics in the last few years. As illustrated in Fig. 1, the rubber is obtained by mixing a monomer (A) and its cross-linking agent (B). The liquid can be vacuumed for air bubble removal (not performed here). Next, the mix is poured onto a mould, here consisting of a flat surface with rigid walls forming a 60-cm-side square. For a 3-mm-thick Ecoflex® plate, one roughly needs 500 ml of each liquid. The mixture is then left for curing at room temperature for several hours until a translucent soft material is obtained. Here, the monomer and its cross-linking agent are mixed in equal quantities. Finally, the shear modulus μ of the obtained elastomer is approximately 25 kPa, according to the datasheet, and checked with a tensile test.

Anticipating ulterior image processing operations, dark pigments are seeded on the polymer during the curing stage. A good contrast is obtained by using small black carbon powder from a local art shop. The seeding operation can be performed after pouring half of the total volume ($t=10$ min) and before pouring the other half (Fig. 1). In the end, one gets a single layer of pigment located halfway through the plate. In this study, the grain density is approximately 1 grain/mm^2.

2. Experimental setup

The experiment consists in shaking the plate and imaging its in-plane motion. To this end, the soft plate is clamped at its top and bottom extremities into a metallic structure (Fig. 2) whose dimensions can be adjusted to avoid static tension, except from gravity.

The excitation is performed by a shaker (TIRAvib 51120, TIRA, Schalkau, Germany), driven by an external arbitrary wave generator (AWG 33 220, Keysight, Santa Rosa, CA), which is itself connected to a power amplifier (analog amplifier BAA 500, TIRA). Typical excitation frequencies span from 1 to 300 Hz. The shaker is connected to a plastic clamp holding a pair of aluminum rods placed on both sides of the soft plate. The two bars pinch the plate over a 30 cm length, ensuring the generation of plane-like waves. The shaker and the pinching rods can be rotated to promote specific polarizations. The setup essentially captures displacements parallel to the (x_1, x_2) plane. As a consequence, it is crucial to carefully align the vibration axis of the shaker with the plate to avoid spurious out-of-plane contributions. The motion is captured by a charge coupled device (CCD) camera (acA4112-20um, Basler, Ahrensburg, Germany) with a 4112×3008-pixel sensor (Fig. 2).

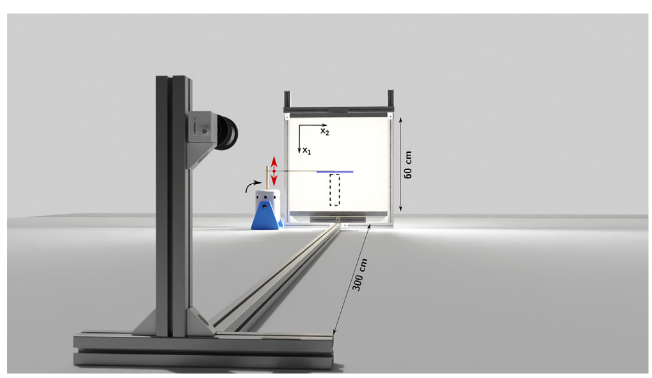

FIG. 2. (Color online) Experimental setup using a line source. A thin plate of Ecoflex® with dimensions 60 cm $\times$ 60 cm $\times$ 3 mm is clamped to an adjustable frame on its top and bottom edges and held in a vertical position. Vibrations are generated by a shaker driven monochromatically. Both the vibration direction and the source orientation can be adjusted to excite different polarizations. The experiment is recorded using a CCD camera located 3 m away from the plate.

Note that it is necessary to use a global shutter: all pixels are exposed simultaneously and capture a full snapshot of the scene. An 85-mm zoom lens mounted on the camera and placed 3 m away from the object provides a clean field of view of a roughly 30-cm-wide square. Narrow angle lenses drastically reduce optical distortions. For an optimal contrast, the system is backlighted with a wide LED panel placed behind the plate.

3. Monochromatic excitation and stroboscopy

Given the chosen region of interest, the maximum acquisition frame rate of the camera is of roughly 130 Hz. This means that Shannon's criterion is not fulfilled for frequencies higher than 65 Hz. However, in the linear regime, there is no need for a higher speed camera since stroboscopic effect can be exploited. To that end, the acquisition period of the camera T_{cam} is set slightly greater than the excitation period $T_{\text{excitation}}$, i.e., $T_{\text{cam}} = T_{\text{excitation}} + \delta t$. Between two successive snapshots, the field undergoes more than a full oscillation period, yet the accumulated phase shift $2\pi\delta t/T_{\text{excitation}}$ remains small. The final movie provides the illusion than the successive snapshots belong to a single wave period (sketch in Fig. 3). We refer to this quantity as the pseudo-period.

For the following post-processing steps, it is preferable to work with a given number of images per movie. The measurements are performed setting this quantity to $N = 60$ frames over one pseudo-period. This means that the acquisition frame rate has to be determined for each different excitation frequency. If the maximum frame rate of the camera is too low, one can always reduce the sampling frequency by waiting for several excitation periods between successive camera triggers. For example, at 100 Hz, an acquisition sampling rate of precisely 24.8963 Hz would yield 60 frames regularly spaced within one pseudo-period (the 61st should be the same as the first image), and successive shots occur roughly every four periods. Note that the exposure time of the camera should always remain much smaller than the excitation period. The image would be blurred otherwise. Our measurements are performed with a typical exposure time of 150 μs. The image quality is seriously hampered above approximately 300 Hz.

In addition to these N frames, a reference image should be captured as the sample is at rest for image processing purposes.

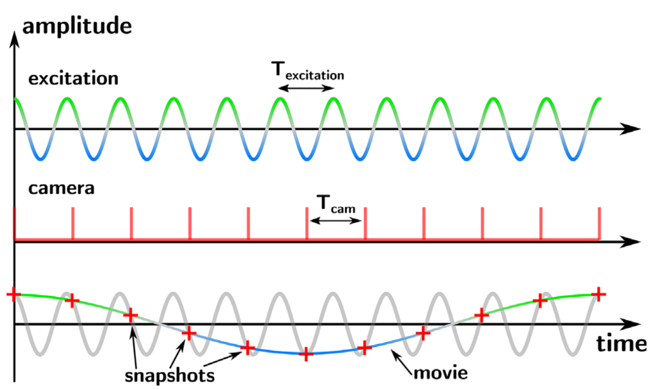

FIG. 3. (Color online) Principle of the stroboscopic imaging. As the recording frame rate is lower than the excitation frequency, one full cycle is reconstructed from the measurements, depicted by the red crosses, taken over several cycles of excitation. The sampling rate has to be precisely defined with respect to the driving frequency.

4. Extraction of the complex displacement maps

Next, each of the N frames is compared to the reference by use of an open source digital image correlation (DIC) algorithm,[35,36] which provides the instantaneous displacement (Fig. 4). The correlation is computed on small image regions, called *macropixels*. Each macropixel yields one displacement vector (u_1, u_2). By repeating the operation for all the macropixels of a single frame, two displacement maps are obtained [Figs. 4(e) and 4(f)]. The macropixel size is set manually. It should be large enough to contain several seeds while remaining smaller than the wavelength. Here, macropixels extending over 25 pixels $\times$ 25 pixels of the original image are chosen, i.e., a size of 2.5 mm. Sometimes, the algorithm fails to find a realistic solution for a given macropixel. In that case, one can always spatially interpolate the missing information or apply a spatial convolution filter to smooth the displacement maps. Note that the DIC algorithm enables sub-pixel resolution. For example, displacements down to 5 μm are measured when a single image pixel corresponds to 100 μm on the plate.

The knowledge of the displacement maps gives the opportunity to build a magnified version of the deformed image as in Fig. 4(c). This can be very useful for visualizing the propagation of waves or for teaching. For communication through writing as in this article, a separate representation of the two components of the displacement as a color code [Figs. 4(d) and 4(e)] is preferred.

At this stage, for a given excitation pulsation ω, a series of N displacement matrices $\mathbf{u}^{(n)}(\mathbf{r})$ are obtained, where $n \in [0, N-1]$ refers to the frame index. From this series, the complex monochromatic displacement is computed as follows:

$$\mathbf{u}(\mathbf{r}, \omega) = \frac{1}{N}\sum_{n=0}^{N-1} \mathbf{u}^{(n)}(\mathbf{r}) e^{2in\pi/N}. \quad (1)$$

The data contained in 60 memory-consuming frames of thousands of pixels have been reduced to the knowledge of a single complex matrix of a few hundred points.

5. Measured in-plane modes

With the setup of Fig. 2, field maps are acquired in an area of 17 cm $\times$ 2.4 cm below the clamp (dashed area in the same figure). Figure 5 gathers the real parts of the extracted displacements for an excitation frequency of 120 Hz. Three different vibration orientations (vertical, horizontal, and 45°) are investigated, while the 30-cm-wide clamp is maintained horizontal.

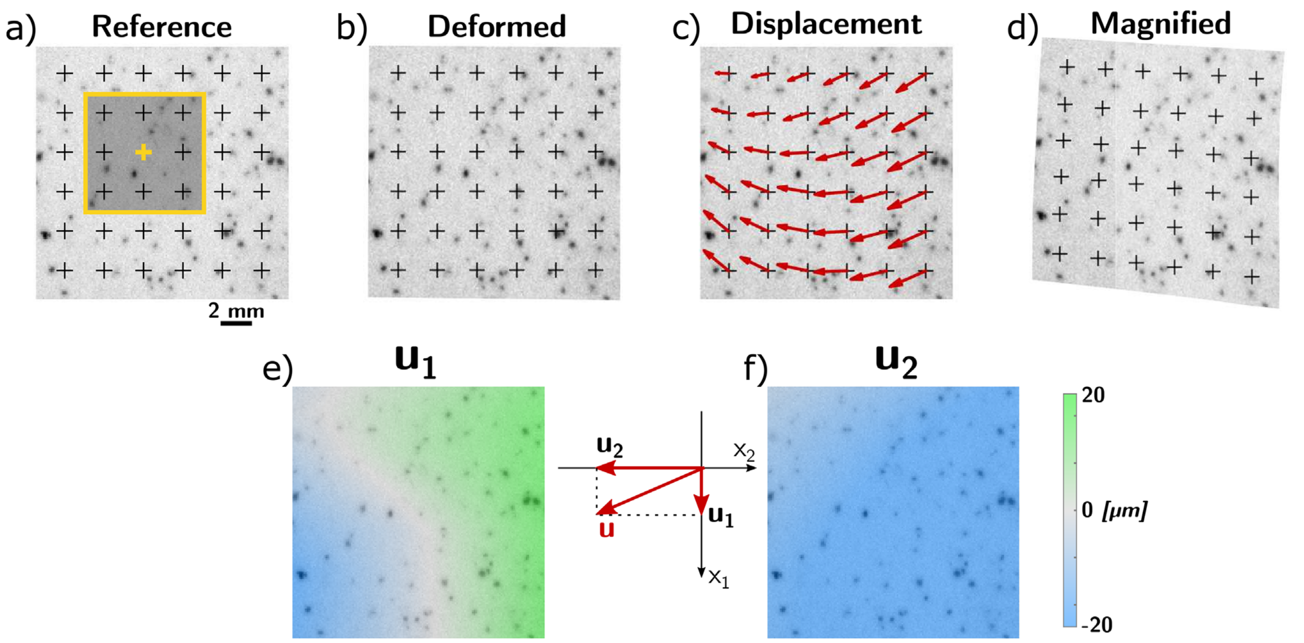

FIG. 4. (Color online) Principle of displacement extraction through a DIC algorithm. (a) Example of a reference image. The black seeds provide a *texture* enabling the DIC analysis. The displacement is computed for each position (crosses) by applying the DIC algorithm over the shaded area. (b) As the shaker is turned on, the image is deformed. The displacements are barely noticeable by eye (typically 10 μm). The DIC algorithm computes the correlation between the deformed and the reference images. (c) Output of the DIC algorithm. A displacement vector is computed for each macropixel. (d) This displacement is used to build a magnified distorted image where displacements appear clearly. The motion is magnified by a factor of 50. [(e) and (f)] Vertical (respectively, horizontal) displacement maps.

In the left part of the Fig. 5, for which the vibration is vertical, u_2 cancels everywhere in the measured area: the motion is purely vertical (along the x_1 axis). Also, u_1 exhibits a periodic pattern along the x_1 direction and a flat profile along the x_2 direction, and the phase travels toward the bottom (not shown here). This measurement corresponds to a plane wave-like pattern (with a wavelength λ of roughly 10 cm) with both the displacement and the wavevector being parallel to x_1. The plate thus supports an in-plane guided elastic wave that we can qualify as longitudinal. Similarly, the horizontal excitation along the x_2 axis of the clamp (middle column in Fig. 5) generates a plane wave-like propagation with a polarization parallel to x_2, that can be qualified as a transverse wave. Interestingly, its wavelength is exactly half the wavelength of its longitudinal counterpart. The versatility of this experimental platform is highlighted in the right panel of Fig. 5. Indeed, instead of selectively exciting each type of plane wave, a motion of the clamp along a 45° tilted direction excites simultaneously the two waves: with one measurement, several modes can be retrieved.

Finally, a systematic extraction of the two aforementioned plane waves for frequencies ranging from 50 to roughly 300 Hz is performed. For each frequency, the

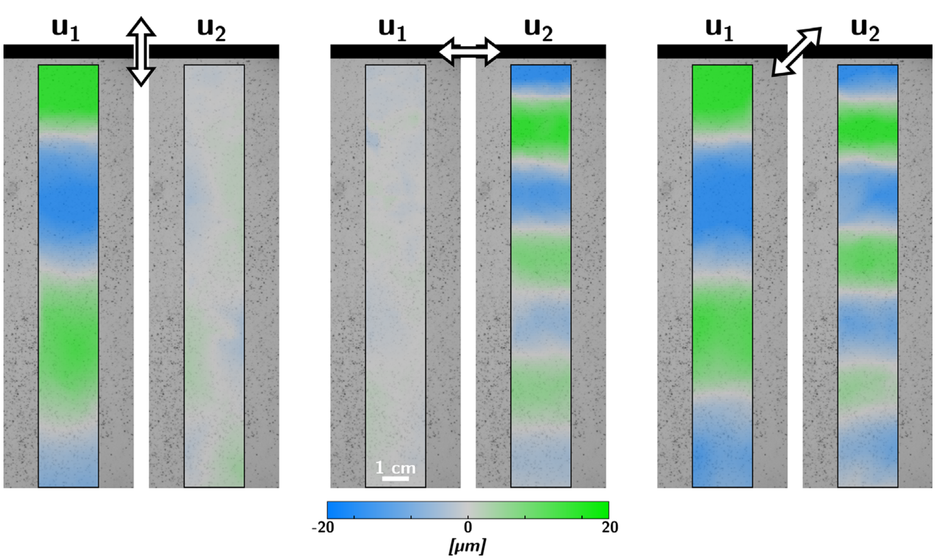

FIG. 5. (Color online) Measurement of in-plane waves in a soft plate. Displacement fields in both vertical (u_1) and horizontal (u_2) directions were measured for three excitation directions with a forcing frequency $f = 120$ Hz. The source oscillates vertically (left), horizontally (middle), or at 45° (right) as indicated by the white arrows. The color bar indicates the magnitude of the in-plane displacements in the elastic plate.

maps are averaged along the x_2 axis, meaning projected onto a plane wave. Then the maximum of the spatial Fourier transform of the profile along x_1 provides the wavenumber $k = 2\pi/\lambda$ (with λ the wavelength) of a mode. This way, a dispersion diagram (i.e., frequency as a function of wavenumber) is constructed for the two polarizations in Fig. 6. Both the dispersion curves appear to be straight lines passing through the origin. They correspond to a non-dispersive propagation, i.e., a propagation at a constant phase velocity. The factor of 2 between the wavelengths here appears as a factor of 2 between the two slopes: the longitudinal mode travels twice as fast (12 m/s) as the transverse one (6 m/s).

In the higher part of the measured frequency range, the experimental points slightly move off the linear behavior. The rheology of the polymer is the origin of this deviation, as explained in Sec. III C, but it remains anecdotal at this stage.

B. Theoretical background

These observations can be explained with a simple theoretical description. The propagation of elastic waves in isotropic solids is a well-documented topic. Comprehensive developments can be found in textbooks.[25,37]

1. Bulk waves

The elastodynamics of a homogeneous isotropic solid requires the knowledge of at least two elastic moduli. For historical reasons, people usually refer to the Lamé constants λ and μ.[38] However, these two constants can be substituted by any other couple of elastic coefficients, such as the Young modulus E, the bulk modulus K, or the Poisson's ratio ν. The case of nearly incompressible media

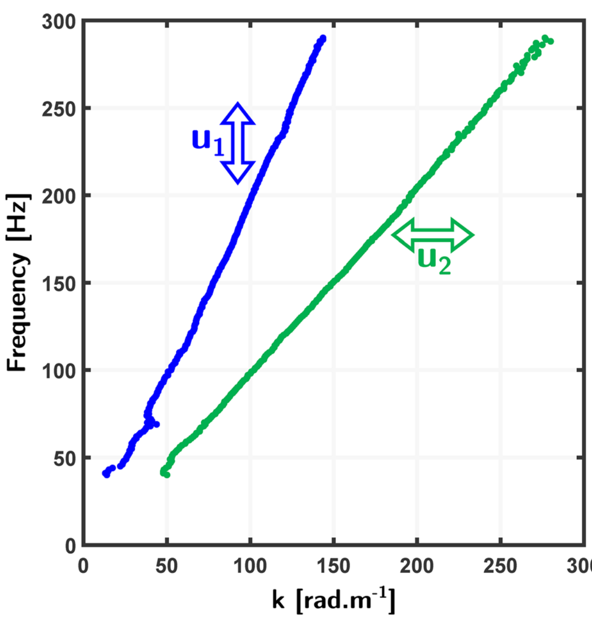

FIG. 6. (Color online) Experimental dispersion curves of in-plane modes in a 3-mm-thick soft plate. A vertically polarized (blue) and a horizontally polarized (green) non-dispersive mode are retrieved. The vertically polarized mode propagates twice as fast as the horizontally polarized one.

corresponds to the limit when $\nu \to \frac{1}{2}$. Knowing that $\nu = \lambda/(2(\lambda+\mu))$, this amounts to $\lambda \gg \mu$ in terms of the Lamé constants.

By combining Newton's law of motion and Hooke's law applied to an infinitesimal volume, one finds that the local displacement field $\mathbf{u}(\mathbf{r}, t)$ obeys the following vector wave equation:

$$\rho \frac{\partial^2 \mathbf{u}}{\partial t^2} = (\lambda+\mu)\nabla(\nabla \cdot \mathbf{u}) + \mu \Delta \mathbf{u}, \tag{2}$$

where ρ stands for the mass density of the solid, and ∇ is the gradient operator. In this equation, the three components of the displacement field are coupled. To decouple the equations, it is common to introduce the scalar potential ϕ and the vector potential $\mathbf{\Psi}$ as

$$\mathbf{u} = \nabla\phi + \nabla \times \mathbf{\Psi}. \tag{3}$$

The component $\nabla\phi$ corresponds to an irrotational vector field, while the component $\nabla \times \mathbf{\Psi}$ is associated with a divergence free field, i.e., a deformation without any volume change. These two potentials are independent and satisfy the following decoupled wave equations:

$$\frac{\partial^2 \phi}{\partial t^2} - \frac{\lambda + 2\mu}{\rho}\Delta\phi = 0, \tag{4}$$

$$\frac{\partial^2 \mathbf{\Psi}}{\partial t^2} - \frac{\mu}{\rho}\Delta\mathbf{\Psi} = 0. \tag{5}$$

These d'Alembert equations confirm the propagation of two different types of waves with distinct polarizations and velocities. On the one hand, Eq. (4) corresponds to a longitudinal wave propagating at velocity $V_L = \sqrt{(\lambda+2\mu)/\rho}$ and with a displacement parallel to the propagation direction. On the other hand, Eq. (5) stands for transverse (or shear) waves propagating at the velocity $V_T = \sqrt{\mu/\rho}$ with displacements perpendicular to the propagation direction. Ecoflex® 00–30 has a measured[39] longitudinal velocity of approximately 1000 m/s, while the shear wave velocity is about 5 m/s. This high contrast between the two velocities ($V_L \gg V_T$) confirms its incompressible nature as

$$\nu = \frac{{V_L}^2 - 2{V_T}^2}{2\left({V_L}^2 - {V_T}^2\right)} \approx \frac{1}{2}. \tag{6}$$

2. Reflection at a free interface

The problem of reflection at an interface reveals the richness of the elastodynamics. Consider an incident plane wave propagating in the plane (x_1, x_3) impinging on a medium interface at $x_3 = 0$ [Fig. 7(a)]. As elastic waves have three polarizations, the reflection at the interface gives rise to three different plane waves. However, the so-called SH wave with displacement along the x_2 direction ($u_1 = u_3 = 0$) can only be generated as a reflection of a SH wave as sketched in Fig. 7(a). On the contrary, longitudinal and SV waves (by

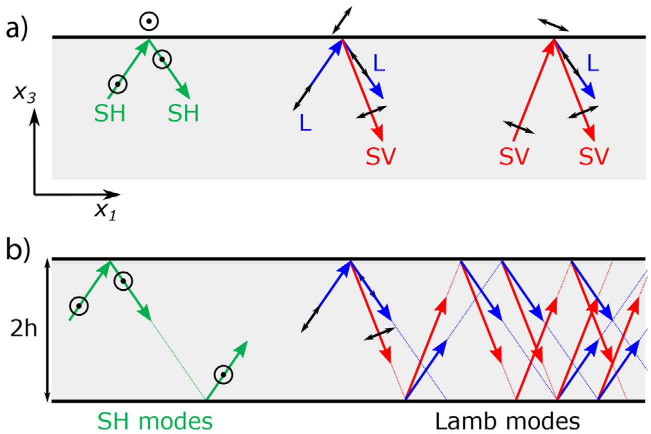

FIG. 7. (Color online) Reflection at a free interface and mode coupling. (a) Reflection of a shear horizontal (SH) wave at an interface does not generate out-of-plane displacements, while longitudinal (L) and shear vertical (SV) waves couple. (b) When multiple reflections occur, SH waves remain independent, while L and SV waves couple, leading to a new family of modes, namely, Lamb waves.

opposition to the SH ones) with displacements in the plane (x_1, x_3) are coupled through reflections at the interface.

Reflection at one interface is the entrance door to more complicated wave phenomena, and notably waveguiding that occurs as a second interface, parallel to the first one, is added. As sketched in Fig. 7(b), the separation between the SH waves and the two others remains valid in this configuration. Sections II B 3 and II B 4 describe the two families of modes that can propagate in a soft plate of thickness $2h$.

3. SH guided waves

The case of SH guided waves is relatively simple because their dispersion curves map those of the well-known acoustic waveguides. Indeed, as all displacements occur along the x_2 axis, the problem becomes a scalar wave problem. Applying the translational invariance along the x_1 axis, one seeks monochromatic solutions of the form

$$\mathbf{u}(\mathbf{r},\omega) = \begin{pmatrix} 0 \\ u_2(x_3,\omega) \\ 0 \end{pmatrix} e^{ikx_1}. \tag{7}$$

Assuming that the interfaces at $x_3 = \pm h$ are free to move, the stress component T_{23} at these interfaces vanishes,

$$T_{23}(x_3 = \pm h) = \mu \left.\frac{\partial u_2}{\partial x_3}\right|_{x_3=\pm h} = 0. \tag{8}$$

Solving the wave equation [Eq. (2)] for shear waves together with these boundary conditions provides the solutions for the guided SH waves inside the plate,

$$u_2(x_3,\omega) = C \cos\left(\frac{n\pi}{2h}(x_3 - h)\right), \tag{9}$$

where C is a scalar constant. And the dispersion relation simply writes

$$k^2 = \left(\frac{\omega}{V_T}\right)^2 - \left(\frac{n\pi}{2h}\right)^2. \tag{10}$$

Such a dispersion relation (Fig. 8) exhibits a non-dispersive mode, denoted SH_0, propagating at all frequencies at the shear velocity V_T, as well as dispersive propagating modes above their respective cutoff frequencies of $f_{c_n} = nV_T/4h$. For a thickness of 3 mm and a shear velocity of roughly 5 m/s, the first cutoff frequency is at 833 Hz, far above the measured frequencies in the experimental part. Thus, the displacement field displayed in Fig. 5 polarized along the x_2 direction corresponds to this SH_0 mode. This transverse mode has already experimentally demonstrated its non-dispersive nature in Fig. 6 (green line).

4. Lamb waves

Due to the coupling at each reflection, the case of longitudinal waves and SV ones is more complicated. However, the calculation steps to establish the dispersion relation and the solutions remain similar. Here, it is preferable to start back from the scalar and vector potentials ϕ and $\boldsymbol{\Psi}$. Applying some geometrical arguments, their expressions can be simplified. First, the invariance by translation along x_1 implies the dependence on x_1 to be on the form e^{ikx_1}. Second, the component of the displacement u_2 is zero, and the other components should not depend on x_2. Third, the plane $x_3 = 0$ is a symmetry plane, so the solutions should be either symmetric or anti-symmetric. Considering all of these simplifications and solving the wave equations [Eqs. (4) and (5)], their analytical formulations write

$$\begin{cases} \phi(\mathbf{r},\omega) = \phi_0 \cos(px_3 + \alpha)e^{ikx_1}, \\ \boldsymbol{\Psi}(\mathbf{r},\omega) = \psi_2 \sin(qx_3 + \alpha)e^{ikx_1}\mathbf{x_2}, \end{cases} \tag{11}$$

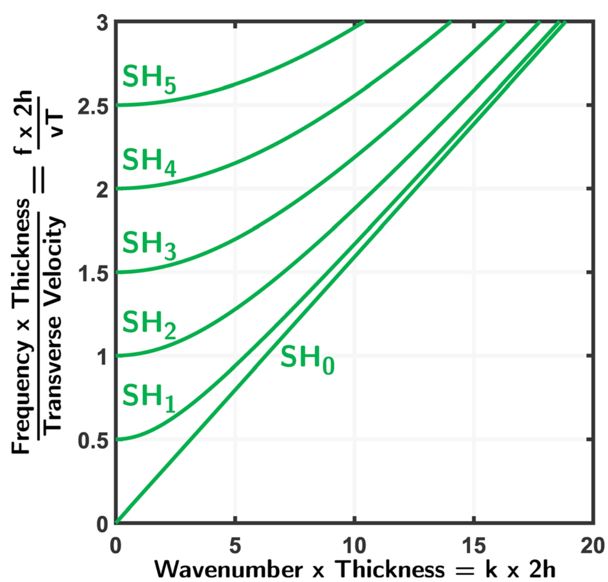

FIG. 8. (Color online) Theoretical dispersion curves of SH waves. The SH_0 mode is non-dispersive with a velocity V_T, while higher modes appear at cutoff frequencies corresponding to every multiple of $V_T/4h$.

with $p^2 = (\omega/V_L)^2 - k^2$ and $q^2 = (\omega/V_T)^2 - k^2$. Symmetrical solutions correspond to $\alpha = 0$, and anti-symmetrical ones correspond to $\alpha = \pi/2$. From these potentials, the displacements are now

$$\mathbf{u}(\mathbf{r}, \omega) = \begin{pmatrix} u_1(x_3, \omega) \\ 0 \\ u_3(x_3, \omega) \end{pmatrix} e^{ikx_1}, \tag{12}$$

with the two non-zero components being

$$\begin{cases} u_1(x_3, \omega) = ik\phi_0 \cos(px_3 + \alpha) - q\psi_2 \cos(qx_3 + \alpha), \\ u_3(x_3, \omega) = -p\phi_0 \sin(px_3 + \alpha) + ik\psi_2 \sin(qx_3 + \alpha). \end{cases} \tag{13}$$

The dispersion relation of these modes is deduced from the boundary conditions. Assuming free boundaries at both interfaces $x_3 = \pm h$, the stresses T_{13} and T_{33} must each cancel, which implies

$$\begin{cases} (k^2 - q^2)\phi_0 \cos(ph + \alpha) = 2ikq\psi_2 \cos(qh + \alpha), \\ (k^2 - q^2)\psi_2 \sin(qh + \alpha) = 2ikp\phi_0 \sin(ph + \alpha). \end{cases} \tag{14}$$

Non-trivial solutions for ϕ_0 and ψ_2 are found when the determinant of this system vanishes. Under these circumstances, u_1 and u_3 are described with a single scalar coefficient C as

$$\begin{cases} u_1(x_3, \omega) = Cq\left[\dfrac{2ik}{k^2 - q^2}\cos(qh + \alpha)\cos(px_3 + \alpha) \right. \\ \qquad\qquad \left. + \cos(ph + \alpha)\cos(qx_3 + \alpha)\right], \\ u_3(x_3, \omega) = iCk\left[\dfrac{2ip}{k^2 - q^2}\cos(qh + \alpha)\sin(px_3 + \alpha) \right. \\ \qquad\qquad \left. + \cos(ph + \alpha)\sin(qx_3 + \alpha)\right], \end{cases} \tag{15}$$

and the dispersion relation, known as the "Rayleigh–Lamb equation," is

$$\begin{aligned} &(k^2 - q^2)^2 \sin(qh + \alpha)\cos(ph + \alpha) \\ &\quad = 4k^2 pq \sin(ph + \alpha)\cos(qh + \alpha). \end{aligned} \tag{16}$$

Unfortunately, the Rayleigh–Lamb equation (Eq. 16) does not have general analytical solutions, and it must be solved numerically. A Muller algorithm[40] is used to find the roots of this equation for the nearly incompressible soft plate considered here. The dispersion curves displayed in Fig. 9 highlight the families of symmetric and anti-symmetric modes. Below the first cutoff frequency of $V_T/4h \approx 833$ Hz, only two modes exist: the anti-symmetric A_0 and the symmetric S_0 modes. While the A_0 dispersion curve is parabolic in the low frequency limit, the S_0 mode is non-dispersive.

The displacements of these modes given by Eq. (15) can also be simplified in the limit $kh \to 0$. For A_0, one finds

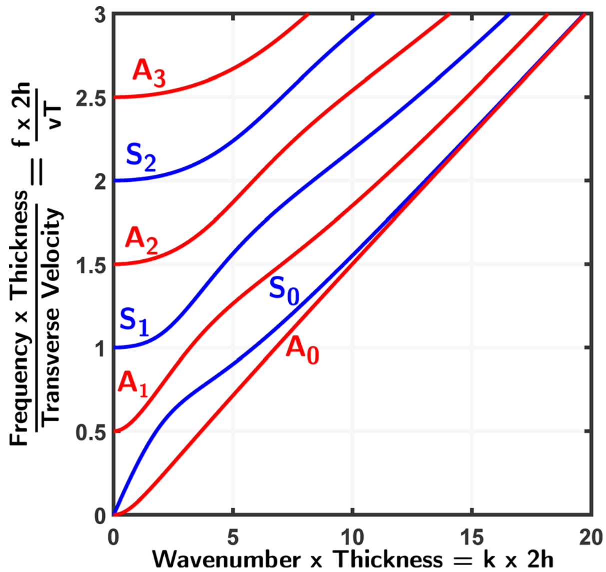

FIG. 9. (Color online) Theoretical dispersion curves of Lamb waves in a nearly incompressible material. Shown are dispersion curves of the symmetric (blue) and anti-symmetric (red) Lamb modes. In the low frequency range, the S_0 mode is non-dispersive with a velocity $V_P = 2V_T$, while the A_0 dispersion curve is parabolic. Higher modes exhibit cutoff frequencies corresponding to every multiple of $V_T/4h$.

$$\begin{cases} u_1(x_3, \omega) = iC'kx_3 + o(k), \\ u_3(x_3, \omega) = C' + o(k), \end{cases} \tag{17}$$

where the new constant C' has been introduced without losing generality. The displacement u_3 is homogeneous across the thickness, and the displacement u_1 is relatively negligible ($kx_3 \to 0$). This mode, generally called flexural mode, is therefore mostly a transverse vertical mode. It is not measured in the previous experiment since the shaker is aligned to avoid out-of-plane displacements.

Taking the limit for the S_0 mode gives

$$\begin{cases} u_1(x_3, \omega) &= C' + o(k), \\ u_3(x_3, \omega) &= iC'kx_3 + o(k). \end{cases} \tag{18}$$

This time, the displacement u_1 is homogeneous across the plate and is far greater than the displacement u_3. In a sense, in this low frequency limit and long wavelength approximation (compared to the thickness), the S_0 mode is seen as a longitudinal mode. Its phase velocity, known as the plate velocity, is given by

$$V_P = 2V_T\sqrt{1 - \left(\frac{V_T}{V_L}\right)^2} = \sqrt{\frac{2}{1-\nu}}V_T. \tag{19}$$

The surprising feature is that, in the incompressible limit, the phase velocity of S_0 simplifies to $V_P = 2V_T$. It is thus independent of the longitudinal velocity V_L despite its apparent longitudinal polarization. This mode corresponds to the measured displacement u_1 presented in Fig. 5, which has twice the wavelength of the SH_0 mode. This analytical derivation now explains the ratio of 2 observed in the experimental dispersion curves in Fig. 6.

III. IN-PLANE GUIDED WAVES IN A SOFT STRIP

In this section, a different geometry is considered: a thin rectangular waveguide made of the same nearly incompressible material. It is obtained by a parallel cutting of the previous plate. First, an analogy is made between this geometry and the plate geometry already described. Notably, the dispersion of in-plane modes propagating in this strip is shown to be similar to the one of Lamb waves propagating in an isotropic plate with a longitudinal wave velocity being exactly twice the shear wave velocity. Then the experimental results already reported in Lanoy *et al.*[34] are presented. The procedure used to separate the modes to obtain their profiles as well as their phase velocities is thoroughly described.

A. Theoretical framework

The theory of elastic modes propagating in rectangular waveguide is not straightforward. As this geometry involves three coupled polarizations, obtaining the full dispersion diagram can be challenging.[41] Thanks to the Rayleigh–Lamb approximation,[42,43] the problem drastically simplifies as one deals with the in-plane modes of a strip with a large aspect ratio. This part addresses this problem in the specific case of a soft solid.

1. Analogy with Lamb waves in a plate

As explained in Sec. II, at low frequencies, only three modes propagate in a plate: the first SH mode SH_0 (Fig. 8) and the symmetric S_0 and anti-symmetric A_0 Lamb modes (Fig. 9). They have uniform profiles across the plate and can roughly be considered as linearly polarized. In particular, S_0 can be seen as a pseudo-longitudinal wave propagating at the constant "plate" velocity V_P. Besides, as shown in Eq. (13), for nearly incompressible materials, the plate velocity is $V_P = 2V_T$. A_0 is essentially polarized along the x_3 axis. As a consequence, it is unaffected by a reflection at the strip edge [Fig. 10(a)]. On the contrary, SH_0 and S_0, which are polarized in the (x_1, x_2) plane, can couple at the edge.

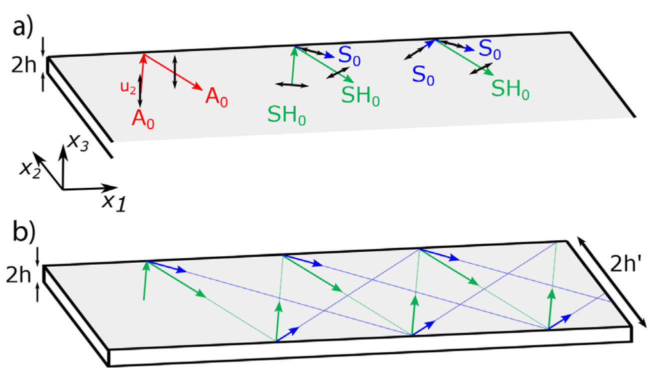

FIG. 10. (Color online) Mode coupling in a strip. (a) The edge reflection of the A_0 mode only generates A_0, while S_0 and SH_0 waves couple. (b) Multiple reflections lead to S_0 and SH_0 in-plane mode coupling in a manner similar to that of shear and longitudinal waves coupling in an infinite plate.

Adding a second edge to form a ribbon of width $2h'$ [Fig. 10(b)], SH_0 and S_0 give rise to in-plane guided modes. As shown in Sec. III of Ref. 42, this coupling is similar to the one of shear and compression bulk waves in a plate. These observations enable us to build an analogy between Lamb waves in a plate and in-plane guided waves in a thin strip. In other words, the dispersion diagram for low frequency in-plane guided waves in a strip is equivalent to the one for guided waves in a plate. In the following descriptions, the prime symbol will be added to the notations when dealing with the strip configuration. The plate thickness $2h$ is replaced by the strip width $2h'$, the longitudinal wave propagating at V_L is replaced by the linearly polarized in-plane wave S_0 propagating at velocity V_P (i.e., $V'_L = V_P$), and the SV wave propagating at V_T is replaced by the transversely polarized in-plane wave SH_0 propagating at V_T (i.e., $V'_T = V_T$), as summarized in Table I.

This amounts to solving the Lamb problem for a material of equivalent Poisson's ratio,

$$\nu' = \frac{\nu}{1+\nu}, \tag{20}$$

where ν is the Poisson's ratio of the strip material. For incompressible materials, the equivalent Poisson's ratio is $\nu' = 1/3$, and the knowledge of V_T is sufficient to obtain the full dispersion diagram of the in-plane guided waves in the low frequency range. Like for Lamb waves, solutions are separated into two families of modes that are either symmetrical (S') or anti-symmetrical (A') with respect to the $x_2 = 0$ plane.

2. Dispersion relation: Key physical features

The dispersion curves of the in-plane modes propagating in a soft strip are thus obtained by finding the roots of the Rayleigh–Lamb equations (Eq. 16). The solutions are displayed in Fig. 11 in normalized units. Several interesting properties deserve to be highlighted.

a. Bar velocity. The first symmetrical mode, denoted S'_0, is approximately non-dispersive for frequencies below the first cutoff frequency. Similarly to the first symmetric S_0 Lamb mode, S'_0 can be seen as a longitudinally polarized mode since it corresponds to a pure compression mode of the ribbon. Its phase velocity can be calculated as a pseudo-plate velocity V'_P. This velocity deduced from Eq. (19) has a remarkably simple formulation,

$$V'_P = \sqrt{\frac{2}{1-\nu'}}V_T = \sqrt{2(1+\nu)}V_T. \tag{21}$$

TABLE I. Analogy between Lamb waves in a plate and in-plane guided waves in a thin strip.

	Guide dimension	Longitudinal velocity	Transverse velocity	Symmetry plane
Plate	Thickness $2h$	V_L	V_T	$x_3 = 0$
Strip	Width $2h'$	$V'_L = V_P$	$V'_T = V_T$	$x_2 = 0$

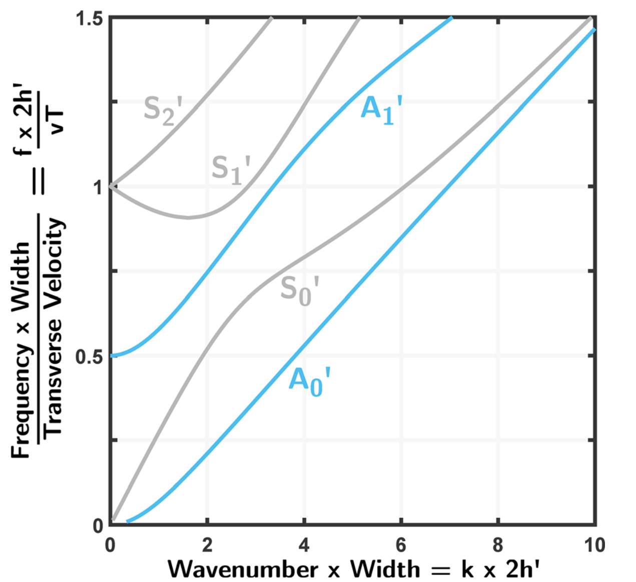

FIG. 11. (Color online) Theoretical dispersion curves of in-plane modes in a soft strip. Shown are dispersion curves of symmetric (gray, labeled S') and anti-symmetric (blue, A') modes without damping. From these curves, one can extract the bar velocity (mode S_0' at low frequencies) and show a ZGV point (S_1') and a backward branch as well as a Dirac cone with a finite group velocity at $k=0$ (at $f=V_T/2h'$).

In the incompressible limit, it simplifies to $V_P' = \sqrt{3}V_T$. Interestingly, although polarized longitudinally at low frequencies, the S_0' velocity only depends on the transverse velocity. This is all the more striking as, in the incompressible limit, the transverse velocity happens to be several orders of magnitude smaller than the longitudinal velocity.

Furthermore, V_P' also corresponds to the well-known bar velocity, associated with the propagation of compression waves along any bar or rod regardless of their cross section. It can be obtained from intuitive reasoning. As it corresponds to a longitudinal extension of the waveguide, the relevant elastic modulus is the Young's modulus E, and the associated velocity is $\sqrt{E/\rho}$. After injecting the expression $E = 2(1+\nu)\mu$, one immediately gets Eq. (21). For a soft material, the Young's modulus simplifies to $E = 3\mu$, and the bar velocity again appears independent of V_L.

b. ZGV and negative phase velocity. Like for Lamb modes, the second symmetrical mode S_1' has a remarkable behavior. Indeed, the corresponding branch exhibits a local minimum for a finite wavenumber. At this specific location, the group velocity $V_g = \mathrm{d}\omega/\mathrm{d}k$ vanishes. This is the signature of a ZGV point. For small wave numbers, the S_1' branch has a negative slope. This indicates that the group velocity is opposite to the phase velocity. Causality imposes that the energy travels from the source to the receiver. As a consequence, the group velocity should always remain positive. In practice, this negative slope section cannot be measured. The experimentalist rather accesses its symmetric branch with respect to the $k=0$ axis. This is further discussed in Secs. III A 2 c and III A 2 d.

c. Dirac cones: Finite group velocity at $k \to 0$. In the small wavenumber limit ($k \to 0$), the branches of the dispersion curve become horizontal (e.g., the Lamb modes in the plate of Fig. 9). The dispersion relation $\omega(k)$ is quadratic around the cutoff pulsation ω_c. As shown by Mindlin,[44] this expansion does not hold for Lamb modes when there is a coincidence between a shear and a longitudinal cutoff frequency of the same symmetry. In these particular cases, the dispersion law is linear in the limit $k \to 0$ and approximates to the first order in k as

$$\omega(k) = \omega_c + V_g k + o(k). \tag{22}$$

Such coincidences occur for symmetrical modes S_{2m+1} and S_{2n}, when the bulk velocity ratio V_L/V_T is equal to $2n/(2m+1)$, and for anti-symmetrical modes A_{2m+1} and A_{2n}, when $V_L/V_T = (2m+1)/2n$. For example, recent experiments conducted in a cooled aluminum plate ($V_L/V_T = 2$) by Stobbe and Murray[45] illustrate this linear dispersion near $k=0$. For modes S_1 and S_2, the linear slopes of the curve $\omega(k)$ can be derived by developing Eq. (16) to the first order, and it was found[44] to be $V_g = \pm 2V_T/\pi$.

The Lamb wave approximation for in-plane modes in a thin soft strip (i.e., $\nu' = 1/3$) reveals a coincidence frequency for the symmetrical modes S_1', S_2'. As a result, these two modes cross linearly at the normalized frequency $f2h'/V_T = 1$ in Fig. 11. This linear crossing is also referred to as a Dirac cone.[46,47]

d. Displacement near the Dirac cone. From Eq. (15), one can determine the displacements close to the cutoff frequencies. For the strip configuration, index 3 must be replaced by 2, h by h', and p by p', such that $p'^2 = (\omega/V_P)^2 - k^2$. The Taylor expansion of coefficients p' and q near the value $k=0$ are

$$\begin{cases} p' = \dfrac{\pi}{2h'} + \dfrac{V_g}{2V_T}k + o(k), \\ q = \dfrac{\pi}{h'} + \dfrac{V_g}{V_T}k + o(k). \end{cases} \tag{23}$$

Using s as the sign of the group velocity, the Taylor expansion of the displacement components at the coordinate point x_2 becomes

$$\begin{cases} u_1(x_2,\omega) = C\dfrac{\pi}{h'}\cos\left(\dfrac{\pi}{h'}x_2\right) + O(k), \\ u_2(x_2,\omega) = -isC\dfrac{\pi}{h'}\sin\left(\dfrac{\pi}{2h'}x_2\right) + O(k), \end{cases}$$

with $s = sign(V_g)$. For ordinary cutoffs, the displacement is either purely longitudinal or purely transverse. Instead, when there is a coincidence, both polarizations are involved. The factor i between the two components denotes an elliptical polarization. At the specific location $x_2 = \pm h'$, the polarization becomes purely circular. The factor s indicates that modes of opposite group velocities are associated with opposite rotation directions.

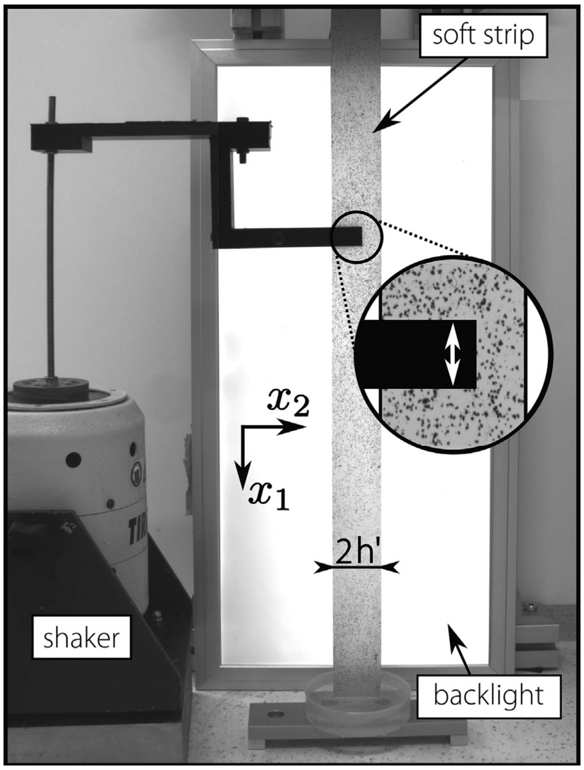

FIG. 12. Experimental setup using a point-like source. A thin strip ($L = 60$ cm, $2h' = 40$ mm, $2h = 3$ mm) is held vertically. A shaker excites in-plane displacements propagating in the strip.

B. Measurements in a soft strip

The soft plate is now replaced with a soft strip. The edges are cut using a laser cutter (Speedy 100 engraver, Trotec, Marchtrenk, Austria). The final strip dimensions are 60 cm, $2h' = 4$ cm, and 3 mm along x_1, x_2, and x_3 directions, respectively. The wide source is replaced with a point-like clamp, obtained by putting two half-spheres in contact. The clamp is slightly off-center and vibrates along the x_1 axis. A picture of the setup[34] is given in Fig. 12.

Here, again, the strip is shaken monochromatically for frequencies ranging from 1 to 200 Hz. The camera captures the motion by following the stroboscopic sketch pictured in Fig. 3. Finally, the displacement field is extracted by applying the DIC algorithm to the successive snapshots. For example, the obtained field maps at 110 Hz are represented in Fig. 13. The wave pattern is rather different from the one obtained in the plate experiment. This comes from a superposition between several modes with different propagation constants and spatial profiles.

Separating and identifying them requires two additional post-processing steps schematized in Fig. 13. First, the symmetrical and anti-symmetrical parts are extracted by, respectively, summing or subtracting the displacement map with its flipped (along the x_2 direction) counterpart. The concatenation of these field maps yields to the construction of two bigger matrices $\mathbf{U}$ (top of Fig. 13), one for each type of symmetry.

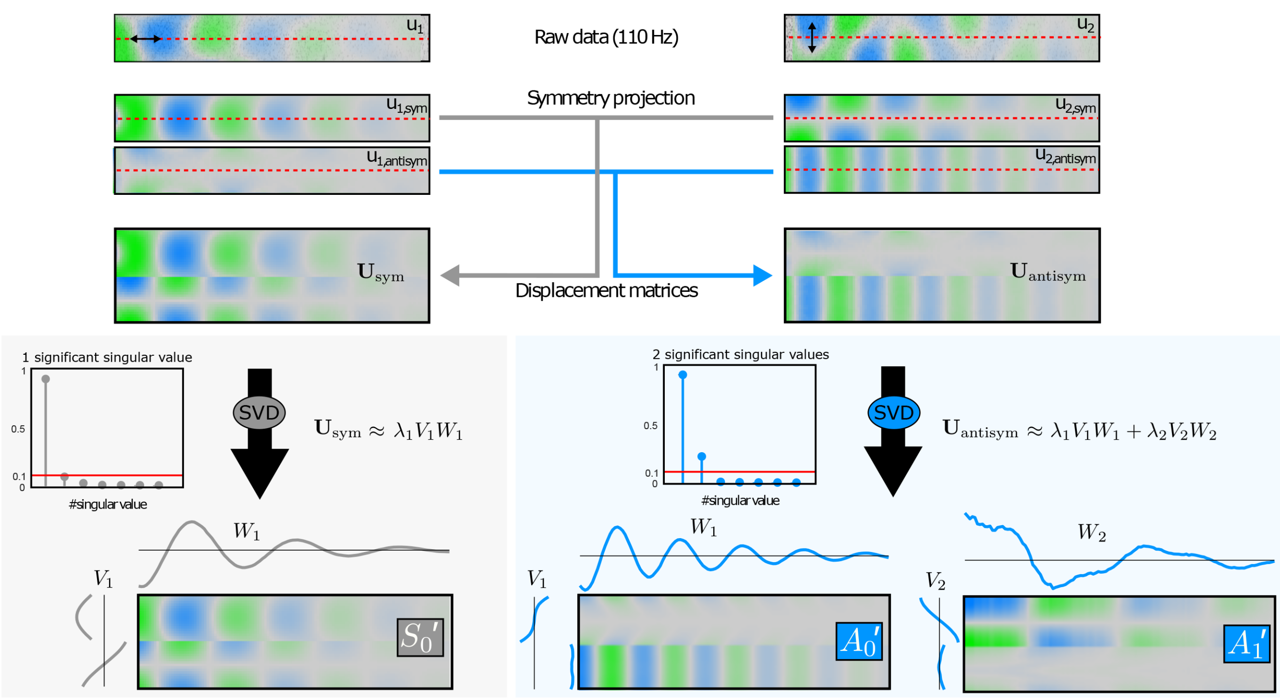

FIG. 13. (Color online) Mode separation via singular value decomposition (SVD). The in-plane displacement components u_1 and u_2 (top left) are projected onto their symmetrical and anti-symmetrical parts (top right). Data are then concatenated into a single complex matrix U_{sym} (respectively, $U_{antisym}$) on which the SVD is directly applied. After extracting the most significant modes (singular values above a 10% threshold), we obtain (here at 110 Hz) one symmetrical (S_0') and two anti-symmetrical (A_0' and A_1') modes.

Then a SVD is performed on each matrix. This amounts to the following matrix decomposition:

$$\mathbf{U} = \mathbf{V}\boldsymbol{\Sigma}\mathbf{W}, \tag{24}$$

where $\mathbf{V}$ and $\mathbf{W}$ are unitary matrices providing the displacement profiles along x_2 and x_1, respectively, and $\boldsymbol{\Sigma}$ is a diagonal matrix providing the singular values (i.e., the mode prominence in the overall measurement). The ith column of $\mathbf{V}$ is noted V_i, and the ith line of $\mathbf{W}$ is noted W_i. As a selection criterion, all modes associated with singular values of at least 10% of the maximum singular value are considered as meaningful. The other ones are rejected. At 110 Hz (see Fig. 13), three modes have a relevant contribution: two symmetrical modes and one anti-symmetrical. Since $\mathbf{W}$ gives the displacement profile along the propagation direction (x_1), its Fourier transform yields the wavenumbers of the contributing modes.

These steps are repeated for all frequencies, and the dispersion curves represented as symbols in Fig. 14 are constructed. As stated earlier, in the experiments, one measures negative phase velocities rather than negative group velocities. This is the reason why the horizontal axis covers negative values.

C. Discussion

Overall experimental dispersion curves in Fig. 14 relatively resemble the theoretical one in Fig. 11, and most of the discussed key features are visible. Indeed, the bar velocity of the strip (mode S'_0 at low frequency) matches the expected value of $\sqrt{3}V_T$ (where V_T is deduced from the SH_0 velocity measured in the plate of Fig. 5). At 150 Hz, S'_2 crosses the axis $k = 0$ with a linear slope: this is a Dirac cone. Note that, below the Dirac frequency, the measured points have negative wavenumbers: this is a signature of a negative phase velocity. The continuity in the measured points naturally leads to labeling this backward branch S'_{2b} ("b" for backward). This may appear to be in contradiction with the dispersion curves for lossless material shown in Fig. 11, where the backward mode belongs to the S'_1 branch. However, when the complex wave numbers are displayed as done by Mindlin for Lamb modes,[48] it clearly appears that the backward branch is connected to S'_2 mode even when the cone does not exist;[44] thus, this notation is adopted in several papers.[29,32,43,49]

However, there are two main differences between the theory in Fig. 11 and the experiment. First, the Dirac cone should be at exactly $2h'/V_T$, but it matches neither the value found from the bar velocity nor the value deduced from the asymptotic behavior at high frequencies of A'_0 and S'_0. Second, the ZGV point is not visible in the experiment. These two differences both originate from the complex rheology of the elastomer.[50]

This rheology is measured with a conventional rheometer (MCR501, Anton-Paar, Graz, Austria), which operates in the plate-plate configuration. To this end, a different sample of Ecoflex® 00–30 is cured in the rheometer itself. Both the real and the imaginary parts of the measured shear modulus for frequencies ranging from 0.1 to 100 Hz are displayed as symbols in Fig. 15. In such a logarithmic scale, the imaginary part of the shear modulus appears linear with a slope of almost 1/3, while the real part seems to increase slowly. Among all the available models, as the slope is not an integer, it balances for a fractional derivative model. One of the simplest models that also satisfies the Kramers–Kronig relations is the fractional derivative Kelvin–Voigt model,[51–53] which takes the form

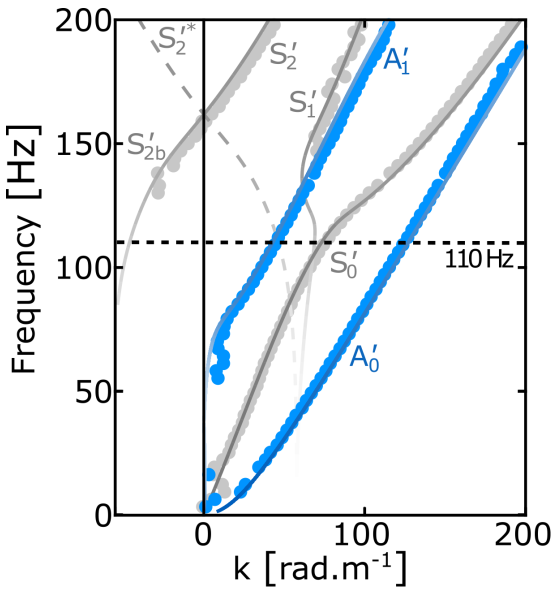

FIG. 14. (Color online) Dispersion curves of in-plane modes in a free strip ($2h' = 39$ mm). Shown are experimental (symbols) and theoretical (lines) dispersion curves with damping (the more transparent the curve, the more attenuated the mode). The Dirac cone (linear crossing of the $k = 0$ axis) and the backward modes (negative wavenumbers) are unambiguously evidenced, while the ZGV point has disappeared. The dashed line denoted by an asterisk is drawn by symmetry and corresponds to a mode propagating in the direction $-\mathbf{x_1}$.

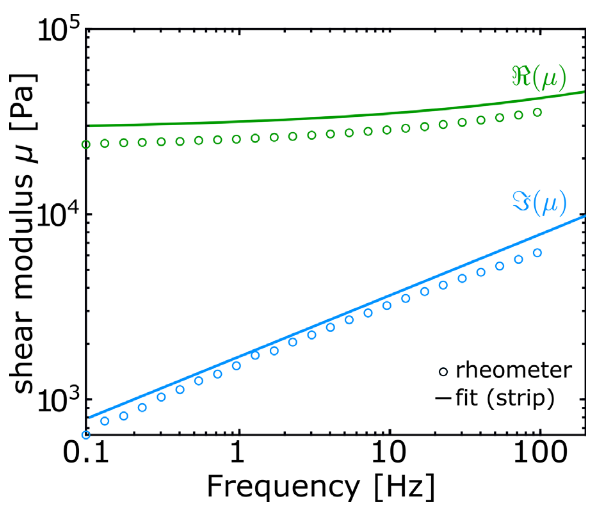

FIG. 15. (Color online) Rheology of Ecoflex®. Shown is measurement of the complex shear modulus of Ecoflex® in the range 0.1–100 Hz with a conventional plane-plane rheometer (circles). $\Re(\mu)$ is the storage modulus of the rubber, while $\Im(\mu)$ is its loss modulus. Lines correspond to the values extracted from the dispersion curves (see the text).

$$\mu(\omega) = \mu_0\left[1 + (\mathrm{i}\omega\tau)^n\right]. \quad (25)$$

This frequency dependent complex shear modulus is injected into the Rayleigh–Lamb equation [Eq. (16)] using a complex transverse velocity $V_T(\omega) = \sqrt{\mu(\omega)/\rho}$. Again, solving this transcendental equation is not an easy task, and its roots are found with the help of an internally developed numerical Muller's algorithm. The latter is run with several sets of parameters of the rheological model until a satisfying agreement between theory and experiment is reached. The final set of parameters is $\mu_0 = 26\,\mathrm{kPa}$, $\tau = 260\,\mu\mathrm{s}$, and $n = 0.33$. It almost corresponds to the measured rheology (Fig. 15) but slightly overestimates $\Re(\mu)$. This discrepancy can be attributed to temperature changes[54] or to differences (preparation or ageing) between the two samples.

The theoretical curves in Fig. 14 are calculated with these parameters. The wavenumber is complex, and its imaginary part is rendered by the transparency of the theoretical lines. The frequency dependence of $\Re(\mu)$ induces a frequency dependence of the velocity V_T, which allows one to fit the entire S_0', A_0', and A_1' branches. Adding the imaginary part of the shear modulus also explains the lowered Dirac frequency. As for the absence of ZGV points, it is solely due to the viscous damping. While for a lossless material, the S_1' branch and the $S_{2b}'^*$ (symmetrical to S_{2b}' with respect to the $k = 0$ axis) connect at the ZGV point, here, the losses separate those two branches.

IV. GOING FURTHER

The fundamental aspects of the system have now been identified. In this section, the experiment is altered to investigate the role of the boundary conditions. In the Dirichlet configuration, the dispersion is found to simplify. After examining the mode polarization, selective excitation is performed by designing specific chiral sources.

A. Investigating Dirichlet boundary conditions

In Sec. II B 4, the analytical Lamb problem is derived assuming free boundary conditions (Neumann configuration). Here, the case of fixed boundaries (Dirichlet configuration) is investigated. In practice, these conditions can be implemented by clamping the strip in a rigid frame (Fig. 16).

1. Theory

a. Dispersion relation. From a theoretical point of view, switching from Neumann to Dirichlet boundaries amounts to replacing the strain cancellation condition of Eq. (14) by a displacement cancellation condition as follows:

$$\begin{cases} ik\phi_0 \cos(p'h' + \alpha) + q\psi_2 \cos(qh' + \alpha) = 0, \\ -p'\phi_0 \sin(p'h' + \alpha) + ik\psi_2 \sin(qh' + \alpha) = 0. \end{cases} \quad (26)$$

The equivalent of the Rayleigh–Lamb equation for rigid boundaries is then

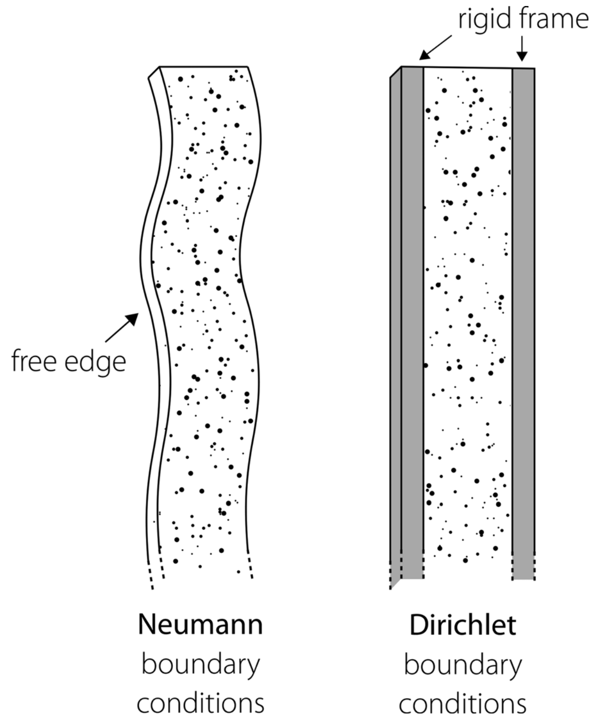

FIG. 16. Boundary conditions. We study the Neumann (free edges) and Dirichlet (fixed edges) boundary conditions.

$$k^2 \sin(qh' + \alpha)\cos(p'h' + \alpha) + qp' \sin(p'h' + \alpha)\cos(qh' + \alpha) = 0. \quad (27)$$

The dispersion curves (Fig. 17) are obtained by searching for the roots of this equation. Compared to the Neumann case (Fig. 11), one important feature is the absence of propagation at low frequency (A_0' and S_0' have disappeared). Indeed, the rigid walls imply that no static in-plane deformation can be the solution to the problem. However, the cutoff modes (A_1', S_1', A_2', etc.) still exist. Note that the negative sloped branch, the Dirac cone, and the ZGV are still visible but for anti-symmetric modes rather than symmetric ones.

Finally, the displacements can be obtained by eliminating the coefficients ϕ_0 and ψ_2 in the boundary conditions of Eq. (26),

$$\begin{cases} u_1(x_2,\omega) = Cq[\cos(p'h' + \alpha)\cos(qx_2 + \alpha) \\ \qquad\qquad + \cos(qh' + \alpha)\cos(p'x_2 + \alpha)], \\ u_3(x_2,\omega) = -iC[k\cos(p'h' + \alpha)\sin(qx_2 + \alpha) \\ \qquad\qquad + p'q\cos(qh' + \alpha)\sin(p'x_2 + \alpha)]. \end{cases} \quad (28)$$

Here, again, the $\pi/2$ phase shift between the two components implies that the motion is elliptically polarized.

b. Dirac cone. The Dirac cone appears here for the anti-symmetric modes at the same frequency $f_c = V_T/2h$ as for the Neumann configuration. At this frequency, the Taylor expansion of p and q are also given by Eq. (23).

JASA
https://doi.org/10.1121/10.0011391

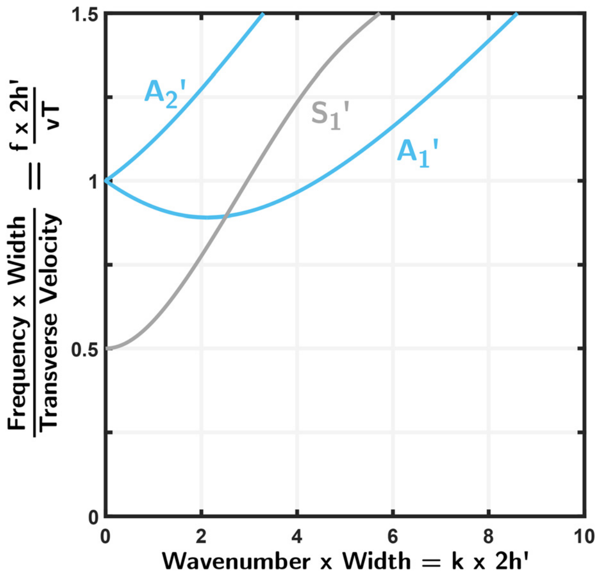

FIG. 17. (Color online) Theoretical dispersion curves of in-plane modes in a clamped soft strip. Shown are dispersion curves of symmetric (gray, labeled S') and anti-symmetric (blue, A') modes without damping. These curves evidence a ZGV point (A_1') and a backward branch as well as a Dirac cone with a finite group velocity at $k=0$ and $f = V_T/2h'$.

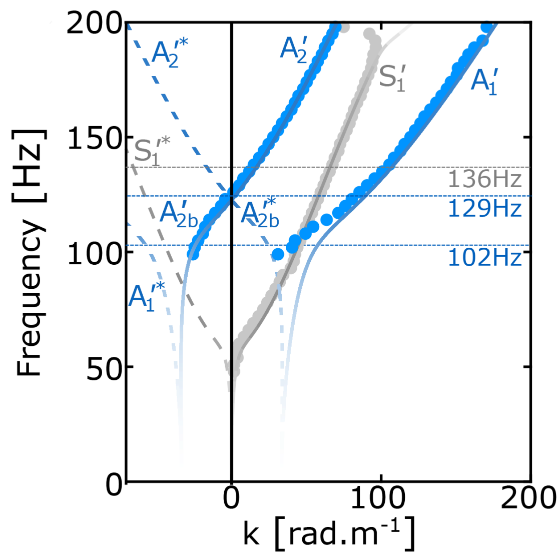

FIG. 18. (Color online) Dispersion curves of in-plane modes in the clamped strip ($2h' = 50.6$ mm). Shown are experimental (symbols) and theoretical (lines) dispersion with damping (the more transparent the curve, the more attenuated the mode). The A_2' Dirac cone (linear crossing of the $k=0$ axis) and the backward A_{2b}' modes (negative wavenumbers) are unambiguously evidenced. The dashed lines labeled with an asterisk correspond to modes propagating in the direction $-\mathbf{x_1}$ and are not measured.

These expressions are substituted into the dispersion relation [Eq. (27)], leading to the same expression for the group velocity $V_g = \pm(2/\pi)V_T$.

Also, Eq. (28) provides the Taylor expansion of the displacements,

$$\begin{cases} u_1(x_2,\omega) & = -\dfrac{\pi}{h'} C \sin\left(\dfrac{\pi}{h'}x_2\right), \\ u_2(x_2,\omega) & = is\dfrac{\pi}{h'} C \cos\left(\dfrac{\pi}{2h'}x_2\right), \end{cases} \tag{29}$$

where s indicates the sign of the group velocity. As $\cos(\pi/6) = \sin(\pi/3)$, a circular polarization occurs for $x_2 = \pm h'/3$, while it appears at $x_2 = \pm h'$ in the Neumann configuration.

2. Measurements in a clamped soft strip

a. Dispersion. The experiment is performed under the same conditions as before. The strip is held along its edges between two steel plates, and the separation between the edges is adjusted to avoid buckling or static tension. The excitation clamp is again slightly off-center and vibrates along the x_1 axis from 40 to 200 Hz. The same image analysis as in the free edges configuration allows extraction of the experimental dispersion curves represented as symbols in Fig. 18. The three modes expected in the measured frequency range are retrieved, and the same observations as in the free strip configuration can be made. First, the data points around 129 Hz show a linear crossing of the axis $k=0$, which evidences the existence of a Dirac cone for the anti-symmetric modes. Second, points measured below this cutoff frequency correspond to negative wavenumbers, which is the signature of a backward mode. Here, again, the continuity of the points across the Dirac cone logically leads to attribution of the backward modes to the branch A_2', unlike what is indicated for the lossless medium theoretical curves (Fig. 17). This part of the curve is thus referred to as A_{2b}'.

Just like for the Neumann configuration, the theory provides a convincing agreement on the condition that the complex rheology of the material is taken into account. The value of $\Re(\mu)$ has an effect on the asymptotic slope of the branches. The value of $\Im(\mu)$ affects the Dirac frequency. In addition, the ZGV point is accurately defined only when $\Im(\mu) = 0$. In this lossy material, two modes with almost opposite wavenumbers coexist, which corresponds to a quasi-ZGV point. The absence of an actual ZGV point is evidenced by the disconnection between branches A_1' and $A_{2b}'^*$. This is a direct consequence of the increase in losses near this point as rendered by the transparency of the lines.

b. Tracking the displacement at the Dirac point. Shaking the strip at 129 Hz (Dirac frequency), the in-plane motion over a complete period was extracted for 25 positions regularly spaced across the strip and located at a distance $x_1 = 18$ cm from the source (far enough to avoid evanescent contributions). After removing the symmetric contribution and specifically selecting the A_2' mode by use of the SVD algorithm, one can reconstruct the full trajectories as shown in Fig. 19(a). They appear to be essentially elliptical and nearly circular at the location $x_2 = \pm h'/3$ (red dashed lines), which is in agreement with Eq. (29).

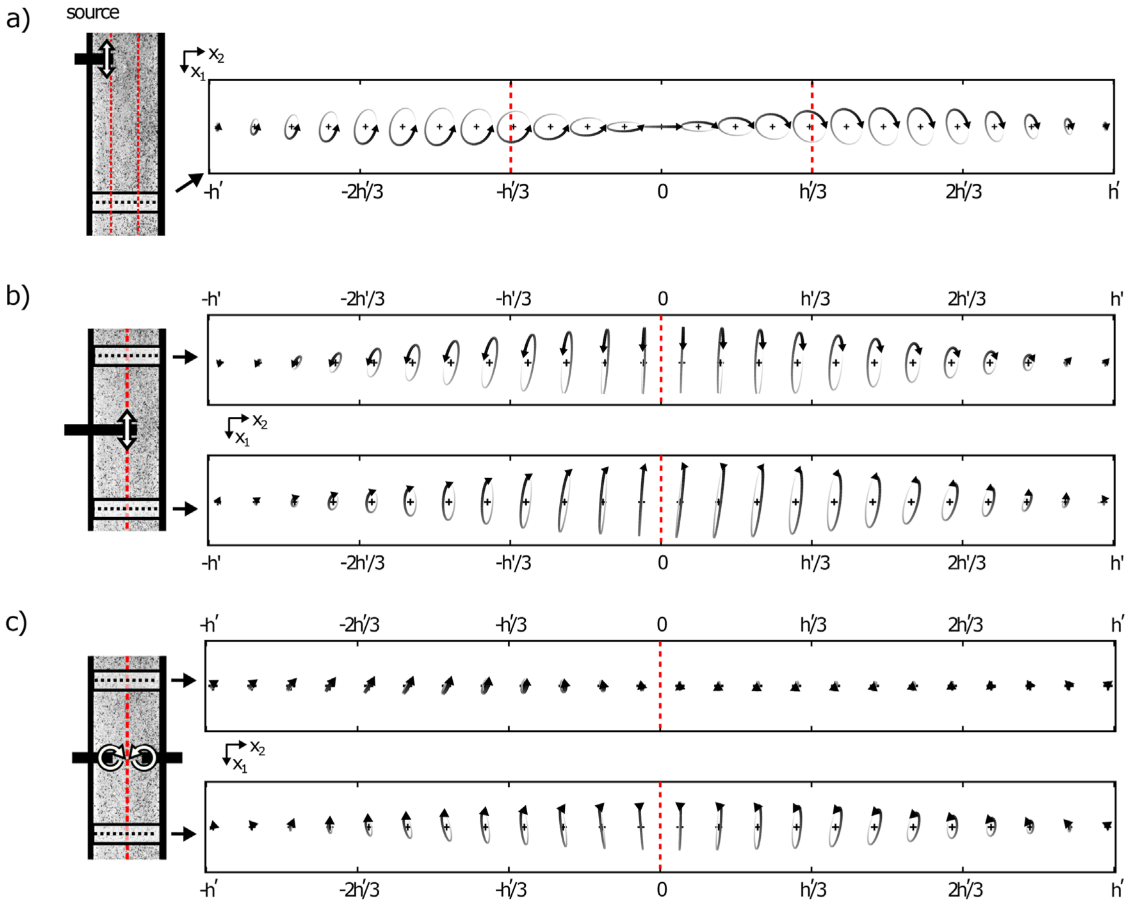

FIG. 19. (Color online) Trajectories. From the instantaneous motion, one can reconstruct the trajectory of a solid element over a full wave period. Here, we specifically display the trajectories of elements distributed along the width of the strip at a distance $x_1 = 18$ cm (a), ± 10.5 cm [(b) and (c)] from the source. The motion is magnified by a factor of 80 (a), 130 (b), and 180 (c). (a) The SVD allows separation of the A_2 contribution and retrieval of the displacement at the Dirac cone (at 129 Hz): a circular motion at positions $\pm h/3$ is observed. (b) For a symmetrical input (at 136 Hz), only the symmetrical mode S_1 and its reciprocal counterpart S_1^*, which propagates in the opposite direction, are excited. (c) A chiral excitation, i.e., two sources placed at roughly $\pm 2h/3$ and driven circularly in a symmetric manner, permits feeding only S_1, and no displacement is measured on the top.

B. Selective excitation

1. One way excitation

In Sec. IV A 2 b, the A_2' mode can be isolated during the post-processing stage (by use of the SVD). Here, the selection is directly performed during the generation stage. Curie's principle states that the resulting wavefield should at least have the same symmetries as the source. As a consequence, a vertically driven source placed in the middle of the strip only feeds the symmetrical modes. The displacements over one cycle for such an excitation at 136 Hz are represented in Fig. 19(b). The only available symmetrical modes at 136 Hz are S_1' for the bottom part and $S_1'^*$ for the top one. The motion is vertical in the center, while it remains elliptical everywhere else as a consequence of the $\pi/2$ phase shift between the two components [Eq. (28)]. However, the rotation directions are different on either side of the source. This is consistent with the fact that S_1' and $S_1'^*$ are phase-conjugate partners.

To exploit this specific polarization, the single vertical source is now replaced by two chiral sources [see Fig. 19(c)], which are rotated in a symmetric fashion. The rotating sources are designed by connecting a clamp to two perpendicular speakers, and the phase quadrature excitation is controlled with a four-channel soundboard (Audiobox 44VSL, Presonus, Baton Rouge, LA). The resulting trajectories [Fig. 19(c)] demonstrate that S_1' is fed but not $S_1'^*$: the top part of the strip remains still. Indeed, the rotation direction of the source corresponds to that of S_1'; it demonstrates how chirality can be used to perform selective excitation. One can get a clearer picture of the phenomenon by examining the field maps. The 12 successive snapshots of the strip over a full wave period are represented next to each other in Fig. 20. The color scale here only indicates the displacement u_1. Just like for Fig. 19(b), when the excitation is purely vertical, S_1' and $S_1'^*$ are fed, and the whole strip is excited [Fig. 20(a)]. As the source becomes chiral, only S_1' is selected: waves travel in the bottom part, while the top part is not excited [Fig. 20(b)].

2. Mode separation

Chiral selection can also be performed with anti-symmetric modes. The strip is now shaken horizontally by two clamps driven simultaneously at 102 Hz (near the quasi-ZGV frequency) following an anti-symmetric scheme. The field

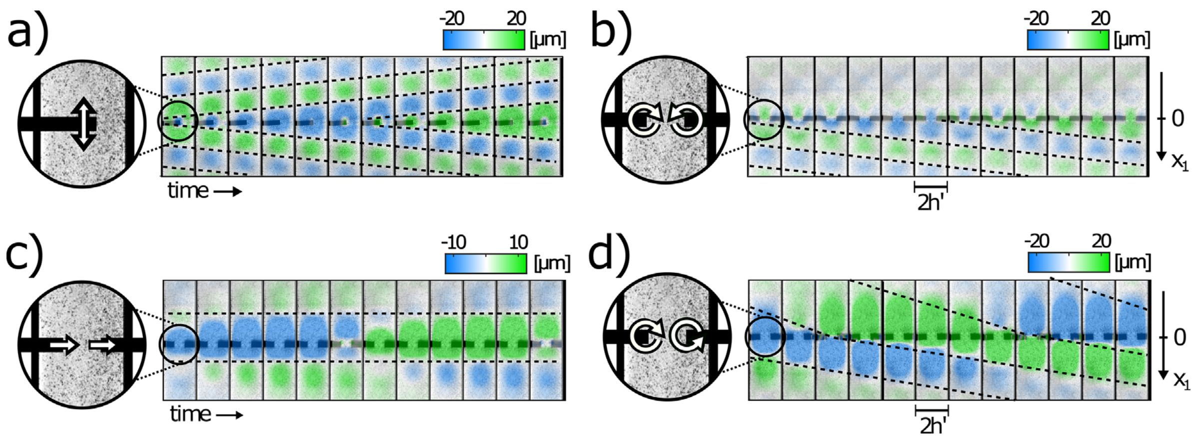

FIG. 20. (Color online) Selective excitation at 136 Hz [(a) and (b)] and 102 Hz [(c) and (d)]. Reprinted with permission from Lanoy *et al.*, Proc. Natl. Acad. Sci. U.S.A. **117**(48), 30186-30190 (2020). Copyright 2020 United States National Academy of Sciences. (Ref. 34). The strip is excited in a symmetrical manner [(a) and (b)] and in an anti-symmetrical manner [(c) and (d)]. The black dashed lines are visual guides highlighting the zeroes of displacement, and the sketches indicate the source geometry and motion. For the sake of clarity, only u_1 [(a) and (b)] or u_2 [(c) and (d)] is reported here. (a) Linear excitation. The source is placed in the center of the strip and shaken vertically: S_1 and S_1^* are excited and travel to the bottom and the top of the strip, respectively. (b) Chiral excitation. Two sources facing each other are rotated in a symmetrical way: the energy is directed toward the bottom, meaning that S_1 is selected. (c) Linear excitation. Two sources are shaken horizontally: a stationary wave is observed. This is the signature of the quasi-ZGV mode. (d) The two sources are rotated, and the wave is propagative. The phase velocity is negative in the top region ($x_1 < 0$) and positive in the bottom region ($x_1 > 0$).

pattern in Fig. 20(c) (which here corresponds to the displacement u_2) reveals a stationary state: the zeroes of displacement remain at the same position over a full excitation period (dashed lines). This is possible only if two waves propagating in opposite directions interfere on both sides of the strip. According to Fig. 18, at this frequency, there are precisely two coexisting modes on either side of the strip: A_1' and A_{2b}' on the bottom part and $A_1'^*$ and $A_{2b}'^*$ on the top part. Near the quasi-ZGV point, their wavenumber magnitudes become similar, meaning that their interferences can give birth to a standing wave.

As depicted in Fig. 20(d), when the clamps are rotated in an anti-symmetrical manner, the wavefield returns to propagative on both parts. And notably, the zeroes travel toward the bottom on both sides (dashed lines). On the upper part, the wave-fronts are backward, i.e., they move toward the source, and therefore correspond to $A_{2b}'^*$. In the bottom part, only A_1' is fed, and the wave-fronts travel away from the source. The chiral excitation has allowed here the separation of the two components of a quasi-ZGV point.

V. CONCLUSION

This article introduces a new "playground" to study wave guiding of elastic waves. It relies on the use of a commercial silicon elastomer. Soft elastomers enable large displacements and slow propagation, which drastically facilitate the experimental procedure. With a few different configurations, we show how this highly visual tool is adequate to explore wave physics phenomena. Furthermore, their quasi-incompressible nature enables the observation of original dispersion effects, such as a Dirac cone.[34] Starting with simple experiments of linearly polarized plane waves propagating in a thin plate, it ends with complex chiral mode selection near a quasi-ZGV mode in a strip with clamped edges. This enables a simple illustration of the theory of a scalar field guided by two interfaces, namely SH modes, to more complex waveguides where two waves with different velocities and polarizations are coupled at each reflection, namely Lamb modes.

The work is not finished, and many other complex guiding geometries can be envisioned. The nearly incompressible nature of the medium being a property shared with most of the biological tissues, analogies with elastic waves existing in the living world can be made. At least three types of wave guides can be identified in the human body. The cochlear wave inside the inner ear of mammalians is supported by the basilar membrane, which resembles the clamped strip studied here. The vocal cords, whose vibrations are responsible for sound control, could be the support of complex stationary fields. Last, arteries or neuronal axons are fluid filled circular soft waveguides also hosting interesting wave phenomena.

ACKNOWLEDGMENTS

This research is supported by LABEX WIFI (Laboratory of Excellence within the French Program "Investments for the Future") under Reference Nos. ANR-10-LABX-24 and ANR-10-IDEX-0001-02 PSL* and by Agence Nationale de la Recherche under Reference No. ANR-16-CE31-0015. A.D. acknowledges funding from French Direction Générale de l'Armement.

[1]I. Levental, P. C. Georges, and P. A. Janmey, "Soft biological materials and their impact on cell function," Soft Matter **3**(3), 299–306 (2007).
[2]M. A. Wozniak and C. S. Chen, "Mechanotransduction in development: A growing role for contractility," Nat. Rev. Mol. Cell Biol. **10**(1), 34–43 (2009).
[3]S. Kumar and V. M. Weaver, "Mechanics, malignancy, and metastasis: The force journey of a tumor cell," Cancer Metastasis Rev. **28**(1), 113–127 (2009).
[4]P. Kalita and R. Schaefer, "Mechanical models of artery walls," Arch. Comput. Methods Eng. **15**(1), 1–36 (2008).
[5]P. R. Murray and S. L. Thomson, "Synthetic, multi-layer, self-oscillating vocal fold model fabrication," J. Vis. Exp. **58**, e3498 (2011).
[6]C. Vannelli, J. Moore, J. McLeod, D. Ceh, and T. Peters, "Dynamic heart phantom with functional mitral and aortic valves," Proc. SPIE **9415**, 941503 (2015).

[7]G. R. Gossweiler, C. L. Brown, G. B. Hewage, E. Sapiro-Gheiler, W. J. Trautman, G. W. Welshofer, and S. L. Craig, "Mechanochemically active soft robots," ACS Appl. Mater. Interfaces **7**(40), 22431–22435 (2015).
[8]L. Marechal, P. Balland, L. Lindenroth, F. Petrou, C. Kontovounisios, and F. Bello, "Toward a common framework and database of materials for soft robotics," Soft Robot. **8**(3), 284–297 (2021).
[9]E. Siéfert, E. Reyssat, J. Bico, and B. Roman, "Bio-inspired pneumatic shape-morphing elastomers," Nat. Mater. **18**(1), 24–28 (2019).
[10]S. Y. Kim, R. Baines, J. Booth, N. Vasios, K. Bertoldi, and R. Kramer-Bottiglio, "Reconfigurable soft body trajectories using unidirectionally stretchable composite laminae," Nat. Commun. **10**(1), 3464 (2019).
[11]L. Sandrin, M. Tanter, J.-L. Gennisson, S. Catheline, and M. Fink, "Shear elasticity probe for soft tissues with 1-D transient elastography," IEEE Trans. Ultrason. Ferroelectr. Freq. Control **49**(4), 436–446 (2002).
[12]J. Foucher, E. Chanteloup, J. Vergniol, L. Castéra, B. L. Bail, X. Adhoute, J. Bertet, P. Couzigou, and V. de Lédinghen, "Diagnosis of cirrhosis by transient elastography (FibroScan): A prospective study," Gut **55**(3), 403–408 (2006).
[13]J.-L. Gennisson, T. Deffieux, M. Fink, and M. Tanter, "Ultrasound elastography: Principles and techniques," Diagn. Interv. Imaging **94**(5), 487–495 (2013).
[14]M. Couade, M. Pernot, C. Prada, E. Messas, J. Emmerich, P. Bruneval, A. Criton, M. Fink, and M. Tanter, "Quantitative assessment of arterial wall biomechanical properties using shear wave imaging," Ultrasound Med. Biol. **36**(10), 1662–1676 (2010).
[15]A. V. Astaneh, M. W. Urban, W. Aquino, J. F. Greenleaf, and M. N. Guddati, "Arterial waveguide model for shear wave elastography: Implementation and *in vitro* validation," Phys. Med. Biol. **62**(13), 5473–5494 (2017).
[16]E. Maksuti, F. Bini, S. Fiorentini, G. Blasi, M. W. Urban, F. Marinozzi, and M. Larsson, "Influence of wall thickness and diameter on arterial shear wave elastography: A phantom and finite element study," Phys. Med. Biol. **62**(7), 2694–2718 (2017).
[17]I. Z. Nenadic, M. W. Urban, S. A. Mitchell, and J. F. Greenleaf, "Lamb wave dispersion ultrasound vibrometry (LDUV) method for quantifying mechanical properties of viscoelastic solids," Phys. Med. Biol. **56**(7), 2245–2264 (2011).
[18]I. Z. Nenadic, M. W. Urban, S. Aristizabal, S. A. Mitchell, T. C. Humphrey, and J. F. Greenleaf, "On Lamb and Rayleigh wave convergence in viscoelastic tissues," Phys. Med. Biol. **56**(20), 6723–6738 (2011).
[19]J. Brum, M. Bernal, J. Gennisson, and M. Tanter, "*In vivo* evaluation of the elastic anisotropy of the human Achilles tendon using shear wave dispersion analysis," Phys. Med. Biol. **59**(3), 505–523 (2014).
[20]H.-C. Liou, F. Sabba, A. I. Packman, G. Wells, and O. Balogun, "Nondestructive characterization of soft materials and biofilms by measurement of guided elastic wave propagation using optical coherence elastography," Soft Matter **15**(4), 575–586 (2019).
[21]J. Griesbauer, S. Bössinger, A. Wixforth, and M. F. Schneider, "Propagation of 2D pressure pulses in lipid monolayers and its possible implications for biology," Phys. Rev. Lett. **108**, 198103 (2012).
[22]M. Hirano, "Morphological structure of the vocal cord as a vibrator and its variations," Folia Phoniatr. Logop. **26**(2), 89–94 (1974).
[23]L. Robles and M. A. Ruggero, "Mechanics of the mammalian cochlea," Physiol. Rev. **81**(3), 1305–1352 (2001).
[24]T. Reichenbach and A. Hudspeth, "The physics of hearing: Fluid mechanics and the active process of the inner ear," Rep. Prog. Phys. **77**(7), 076601 (2014).
[25]D. Royer and E. Dieulesaint, *Elastic Waves in Solids I: Free and Guided Propagation* (Springer, Berlin, 1999).
[26]D. N. Alleyne and P. Cawley, "The interaction of Lamb waves with defects," IEEE Trans. Ultrason. Ferroelectr. Freq. Control **39**(3), 381–397 (1992).
[27]Z. Su, L. Ye, and Y. Lu, "Guided Lamb waves for identification of damage in composite structures: A review," J. Sound Vib. **295**(3), 753–780 (2006).
[28]S. Bramhavar, C. Prada, A. A. Maznev, A. G. Every, T. B. Norris, and T. W. Murray, "Negative refraction and focusing of elastic Lamb waves at an interface," Phys. Rev. B **83**(1), 014106 (2011).
[29]F. D. Philippe, T. W. Murray, and C. Prada, "Focusing on plates: Controlling guided waves using negative refraction," Sci. Rep. **5**, 11112 (2015).
[30]I. Tolstoy and E. Usdin, "Wave propagation in elastic plates: Low and high mode dispersion," J. Acoust. Soc. Am. **29**(1), 37–42 (1957).
[31]S. D. Holland and D. E. Chimenti, "Air-coupled acoustic imaging with zero-group-velocity Lamb modes," Appl. Phys. Lett. **83**(13), 2704–2706 (2003).
[32]C. Prada, O. Balogun, and T. Murray, "Laser-based ultrasonic generation and detection of zero-group velocity Lamb waves in thin plates," Appl. Phys. Lett. **87**(19), 194109 (2005).
[33]C. Prada, D. Clorennec, and D. Royer, "Local vibration of an elastic plate and zero-group velocity Lamb modes," J. Acoust. Soc. Am. **124**(1), 203–212 (2008).
[34]M. Lanoy, F. Lemoult, A. Eddi, and C. Prada, "Dirac cones and chiral selection of elastic waves in a soft strip," Proc. Natl. Acad. Sci. U.S.A. **117**(48), 30186–30190 (2020).
[35]S. Wildeman, "Real-time quantitative Schlieren imaging by fast Fourier demodulation of a checkered backdrop," Exp. Fluids **59**(6), 97 (2018).
[36]S. Wildeman, "swildeman/dicflow," https://github.com/swildeman/dicflow (Last viewed May 2022).
[37]B. A. Auld, *Acoustic Fields and Waves in Solids* (Wiley, New York, 1973).
[38]In the polymer or rheology communities, the Lamé coefficient μ is noted G.
[39]Measured at 3 MHz with a pulse echo method in a bulk sample.
[40]D. E. Muller, "A method for solving algebraic equations using an automatic computer," Math. Comput. **10**, 208–215 (1956).
[41]A. A. Krushynska and V. V. Meleshko, "Normal waves in elastic bars of rectangular cross section," J. Acoust. Soc. Am. **129**(3), 1324–1335 (2011).
[42]M. Cross and R. Lifshitz, "Elastic wave transmission at an abrupt junction in a thin plate with application to heat transport and vibrations in mesoscopic systems," Phys. Rev. B **64**, 085324 (2001).
[43]J. Laurent, D. Royer, and C. Prada, "In-plane backward and zero-group-velocity guided modes in rigid and soft strips," J. Acoust. Soc. Am. **147**, 1302–1310 (2020).
[44]R. D. Mindlin, *An Introduction to the Mathematical Theory of Vibrations of Elastic Plates*, edited by J. Yang (World Scientific, Singapore, 2006).
[45]D. M. Stobbe and T. W. Murray, "Conical dispersion of Lamb waves in elastic plates," Phys. Rev. B **96**(14), 144101 (2017).
[46]A. Maznev, "Dirac cone dispersion of acoustic waves in plates without phononic crystals," J. Acoust. Soc. Am. **135**(2), 577–580 (2014).
[47]X. Huang, Y. Lai, Z. H. Hang, H. Zheng, and C. Chan, "Dirac cones induced by accidental degeneracy in photonic crystals and zero-refractive-index materials," Nat. Mater. **10**(8), 582–586 (2011).
[48]R. D. Mindlin and M. A. Medick, "Extensional vibrations of elastic plates," J. Appl. Mech. **26**(4), 561–569 (1959).
[49]B. Gérardin, J. Laurent, C. Prada, and A. Aubry, "Negative reflection of Lamb waves at a free edge: Tunable focusing and mimicking phase conjugation," J. Acoust. Soc. Am. **140**(1), 591–600 (2016).
[50]Again, in the polymer or rheology communities, the Lamé coefficient μ is noted G, which leads to the real part G' and the imaginary part G''.
[51]F. C. Meral, T. J. Royston, and R. L. Magin, "Surface response of a fractional order viscoelastic halfspace to surface and subsurface sources," J. Acoust. Soc. Am. **126**(6), 3278–3285 (2009).
[52]S. P. Kearney, A. Khan, Z. Dai, and T. J. Royston, "Dynamic viscoelastic models of human skin using optical elastography," Phys. Med. Biol. **60**(17), 6975–6990 (2015).
[53]E. Rolley, J. H. Snoeijer, and B. Andreotti, "A flexible rheometer design to measure the visco-elastic response of soft solids over a wide range of frequency," Rev. Sci. Instrum. **90**(2), 023906 (2019).
[54]Y. Wan, Y. Xiong, and S. Zhang, "Temperature dependent dynamic mechanical properties of magnetorheological elastomers: Experiment and modeling," Composite Struct. **202**, 768–773 (2018).